Atmos. Chem. Phys. Discuss., 5, 67–100, 2005
www.atmos-chem-phys.org/acpd/5/67/
SRef-ID: 1680-7375/acpd/2005-5-67
European Geosciences Union

Atmospheric Chemistry and Physics Discussions

Formation of ice supersaturation by mesoscale gravity waves

P. Spichtinger, K. Gierens, and A. Dörnbrack

Deutsches Zentrum für Luft- und Raumfahrt, Institut für Physik der Atmosphäre, Oberpfaffenhofen, Germany

Received: 4 October 2004 – Accepted: 29 November 2004 – Published: 10 January 2005

Correspondence to: P. Spichtinger (peter.spichtinger@dlr.de)

Abstract

We investigate the formation and evolution of an ice-supersaturated region (ISSR) that was detected by means of an operational radiosonde sounding launched from the meteorological station of Lindenberg on 21 March 2000, 00:00 UTC. The supersaturated layer was situated below the local tropopause, between 320 and 408 hPa altitude. Our investigation uses satellite imagery (METEOSAT, AVHRR) and analyses of the European Centre for Medium-Range Weather Forecasts (ECMWF). Mesoscale simulations reveal that the ISSR was formed by a temporary vertical uplift of upper tropospheric air parcels by 20 to 40 hPa in 1 to 2 h. This resulted in a significant local increase of the specific humidity by the moisture transport from below. The ascent was triggered by the superposition of two internal gravity waves, a mountain wave induced by flow past the Erzgebirge and Riesengebirge south of Lindenberg, and an inertial gravity wave excited by the anticyclonically curved jet stream over the Baltic Sea. The wave-induced ISSR was rather thick with a depth of about 2 km. The wave-induced upward motion causing the supersaturation also triggered the formation of a cirrus cloud. METEOSAT imagery shows that the cirrus cloud got optically thick within two hours. During this period another longer lasting thin but extended cirrus existed just beneath the tropopause. The wave-induced ISSR disappeared after about half a day in accordance with the decaying wave activity.

1. Introduction

Ice-supersaturated regions (ISSRs) in the upper troposphere are generally colder and moister (in the sense of water vapour concentration) than their subsaturated surroundings (Gierens et al., 1999; Spichtinger et al., 2003b). These contrasts reveal information on the probable pathways to supersaturated states. In the case of a temperature contrast to the subsaturated environment it is probably adiabatic cooling by large-scale ascending motion leading to supersaturation. However, in the lowermost stratosphere

ACPD

5, 67–100, 2005

and in the tropical tropopause layer diabatic cooling by radiation can be effective, too. In case of a moisture contrast, smaller scale motions transport moisture from lower levels upward leading to localized supersaturation.

In a companion paper (Spichtinger et al., 2004, hereafter Case 1) we studied the formation of ice-supersaturated regions in the cold upper troposphere over NE Germany. This ISSR was formed by adiabatic cooling in a slowly ascending airmass under the influence of a warm conveyor belt associated with a low pressure system west of Ireland. In this paper, we present a different case where supersaturation was produced by mesoscale gravity waves. The superposition of two distinct wave packets lifted moist air upward within a relatively short time period and over a relatively small area around the meterological station of Lindenberg. An operational radiosonde launched on 20 March 2000, 22:00 UTC detected the ISSR between 408 and 320 hPa altitude.

The meteorological situation was dominated by an anticyclonic breaking Rossby wave which intrudes subtropical air masses into mid-latitudes and polar regions (Fig. 1). The observation of the ISSR took place during an anticyclonic Rossby wave breaking event (P2, after Peters and Waugh, 1996). In the second phase of this event, the extruded air masses wrapped themselves anticyclonically forming a large, quasi-stationary ridge extending from the mid Atlantic toward the North Sea. During the time period considered in this study the ridge slowly expanded towards Central Europe. At the same time, a trough with its centre near the Black Sea propagated southeast and caused a nearly straight northeasterly jet streak between the both pressure centres south of the meteorological station of Lindenberg. North of Lindenberg, the mid-tropospheric flow was dominated by the strongly anticyclonically curved jet stream at the northeast side of the ridge.

In the following section we describe the data sources and techniques applied for the analysis of this case; the analysis itself is presented in Sect. 3. In Sect. 4 we visualise the supersaturation field in the same way as we have done in Case 1, and conclusions are drawn in the final Sect. 5

2. Data handling

As in Case 1 we use a number of data sets that are briefly described in the following; for more details we refer to Case 1.

2.1. Radiosoundings

We use the vertical profiles (pressure, altitude, temperature and relative humidity, RH) from the RS80A radiosoundings, corrected by the Lindenberg research team (see Spichtinger et al., 2003a). Additionally, the horizontal wind (eastward and northward wind components u and v) is available.

2.2. METEOSAT infrared data

We use METEOSAT infrared data and perform simple radiative transfer calculations (see below) with them, in order to distinguish between clear and cloudy air.

2.3. Meteorological analyses and trajectory calculations

Another database for our study are the operational analyses of the European Centre for Medium-Range Weather Forecasts (ECMWF) global assimilation scheme. We use the data with the same horizontal and vertical resolution as in Case 1 (T319L60).

The operational analyses of ECMWF constitute the base for the LAGRangian ANalysis TOol (LAGRANTO, cf. Wernli and Davies, 1997), a three-dimensional trajectory model. This model is driven by the wind fields of ECMWF analyses and allows the calculation of kinematic Lagrangian trajectories.

As the 6 h time interval of the ECMWF data turns out to be too coarse for the analysis of the present case, we perform mesoscale numerical simulations of the situation using the weather prediction model MM5 (Dudhia, 1993; Dudhia et al., 2001) with a time step of 10 s and a minimum grid size of 9 km horizontally and about 150 m vertically. Mesoscale trajectories are calculated using the results of the numerical simulations.

ACPD
5, 67–100, 2005

3. Case study of 21 March 2000

In this section we present the analysis of the data sets mentioned above.

3.1. Radiosonde profiles and ECMWF analyses

In Fig. 2 the vertical profiles for temperature, specific humidity, and relative humidity with respect to ice as obtained from the radiosounding are presented. Additionally, profiles obtained from ECMWF data, the thermal tropopause, and an ice supersaturation layer are shown. The specific humidity (radiosounding) is calculated from the variables temperature (T), pressure (p) and relative humidity with respect to ice (RHi). In the following we only describe the vertical profiles of temperature and relative humidity with respect to ice.

The temperature decreases with height from the surface to about 185 hPa with a few exceptions: At pressure levels 944, 831, 647 and 568 hPa there are temperature inversions. The two lowest temperature inversions indicate the presence of low clouds (boundary layer clouds). The thermal tropopause is situated at pressure level 183.2 hPa.

The relative humidity profile is much more complicated: From the surface to about 938 hPa there is nearly water saturation. Above the first temperature inversion (at 944 hPa) RHi decreases to about 80%, and above the second temperature inversion (at 831 hPa) even to about 30%. Between 800 and 550 hPa there are several local maxima and minima in the RHi-profile (mainly at the temperature inversions). RHi increases strongly between $550 \geq p \geq 300$ hPa and the air is supersaturated in the pressure range $408 \geq p \geq 320$ hPa (with a shallow dip below saturation, namely to 97%). Above the supersaturated layer RHi decreases first, but has another local maximum between 300 and 170 hPa with values at about 90%. Above the tropopause RHi decreases rapidly.

In the following sections we will concentrate on the ice supersaturation layer ($p \approx 420-310$ hPa) and the humid layer just below the tropopause ($p \approx 275-170$ hPa)

ACPD
5, 67–100, 2005

in more detail. The ice supersaturation layer actually consists of two layers (in the radiosounding), because it has embedded in it a slightly subsaturated shallow layer of 150 m thickness. This gap between the supersaturation layers could be an artefact, since the radiosonde underestimates relative humidity when there is ice on the humidity sensor.

We compare the radiosonde profile with the corresponding values from the ECMWF data, retrieved from the nearest grid point to the actual position of the radiosonde (calculated via the wind profile of the radiosonde). The temperature profile obtained from the radiosonde is well reproduced by the ECMWF analysis. However, the temperature inversions are missing as the vertical fine structure is not resolved by the model. The structure of the specific humidity profile (radiosonde) agrees qualitatively with the ECMWF model analyses, but there are quantitative differences: Especially in the pressure ranges 400–170 hPa and 750–600 hPa the ECMWF analyses underestimate the specific humidity.

Also the structure of the RHi-profile is reproduced qualitatively quite well by the ECMWF model. But quantitatively the model profile shows some problems: Due to the underestimation of the specific humidity the relative humidity is also underestimated in the pressure range 400–170 hPa. The maximum in the relative humidity profile is shifted to higher pressures values (i.e. downwards) and, in particular, the relative humidities do not exceed saturation. Nevertheless, the qualitative agreement between the modelled and the measured RHi profiles encourage us to proceed with the analysis based on the ECMWF data.

3.2. Trajectory calculations

3.2.1. Trajectories

The time of the ISSR detection by the radiosonde over Lindenberg on 21 March 2000 00:00 UTC will be referred to as t=0 h and other times will be expressed relative to this date.

We calculate forward (t=0 h→t=+24 h) and backward (t=0 h→t=−36 h) trajectories of air parcels released in a starting region around Lindenberg (14.12° E/52.22° N): longitude 13.2–16.2° E, latitude 51.0–53.4° N, pressure 170–510 hPa (i.e. model levels 29–40). For t=0 h we determine for each model level the nearest grid point to the actual radiosonde position called the main grid point. The trajectory through each of the 12 level-dependent main grid points is called the main trajectory in the following discussion. Additionally, the trajectories through the four adjacent grid points are considered. The trajectories are labelled in the following way: $\mathrm{Tr}_{\ell,i}$, where ℓ denotes the ECMWF level which the trajectory touches at t=0 h. The index i is 1 for the main trajectory and 2–5 for the other trajectories (counted counterclockwise, starting at the northern grid point).

The trajectory pattern was characterized by the anticyclonic flow around the ridge over the North Sea. During the time interval [−36, −6] h the mid-tropospheric westerly wind carried the air parcels over the southern tip of the Scandinavian Alps. A coherent vertical displacement with a peak-to-peak amplitude of ∼70 hPa there occured in all trajectories due to mountain wave activity. In the following time interval [−6, +24] h the air parcel trajectories wrapped anticyclonically around the ridge without significant changes in altitude. Other backward trajectories released further east of Lindenberg (not shown) display a diffluent region at the northeastern edge of the anticyclone in accordance with the flow pattern shown in Fig. 1.

3.2.2. Contributions to the change of relative humidity

Ice supersaturation is analysed on the ECMWF pressure levels 34–36 (i.e. p_{34}≈320 hPa, p_{35}≈345 hPa, p_{36}≈390 hPa). Hence, we calculate the contributions of the variables T, q and p to the change of the relative humidity along the trajectories $\mathrm{Tr}_{34,i}$–$\mathrm{Tr}_{36,i}$. As in Case 1 we assume that a linearisation is possible, i.e. we compute

the total differential

$$dRHi = \frac{\partial RHi}{\partial T}\, dT + \frac{\partial RHi}{\partial q}\, dq + \frac{\partial RHi}{\partial p}\, dp. \quad (1)$$

The result of the calculations suggests ice supersaturation along the trajectories $Tr_{34,i}$–$Tr_{36,i}$ for the timestep $t=-6\,h \rightarrow t=0\,h$ through a large increase of the specific humidity q by a factor of about 1.5 to 1.75. The temperature decreases only marginally during this period.

As explained in the Appendix, a large q-change along a trajectory raises the issue of the realism of the calculated properties of the transported air parcel (cf. also Stohl and Seibert, 1998). Indeed, a closer look to the radiosonde and ECMWF profiles of specific humidity at −6 h and 0 h suggests a vertical uplift of about 30 hPa in the pressure range $220 \leq p \leq 450$ hPa. This significant ascent is not resolved by the trajectories based on 6-hourly wind data. The origin of this quick and supposedly small-scale uplift is not clear from the available data. After testing different hypotheses, we conjecture that the localized ascent was related to internal gravity waves. In order to check this hypothesis we perform a mesoscale simulation which will be discussed in Sect. 3.4. But before this discussion we want to check for cloud presence in the supersaturation layer, which is investigated in the next section.

3.3. Check of cloud presence

In this section we examine the cloud evolution using METEOSAT infrared imagery. Figures 3 and 4 cover the period from 20 March 2000, 17:30 UTC to 21 March 2000, 05:30 UTC. Lindenberg is indicated as a black bullet on these figures. The positions of the air parcels that were crossed by the radiosonde on ECMWF pressure levels 34–36 (i.e. $p_{34} \approx 320$ hPa, $p_{35} \approx 345$ hPa, $p_{36} \approx 390$ hPa) at the nominal time 00:00 UTC are marked on some of the figures as black triangles. These positions are computed from the measured wind data for a time frame of ±3 h around the radiosonde ascent. Additionally, the positions of the main trajectories $Tr_{34,1}$, $Tr_{35,1}$, $Tr_{36,1}$ (start at 13.8° E/52.2° N,

black squares) and the trajectories $Tr_{34,5}$, $Tr_{35,5}$, $Tr_{36,5}$ (start at 14.4° E/52.2° N, black stars) are marked. At 23:00 UTC all these air parcels are so close to Lindenberg that we have only plotted the bullet for this location.

Between 17:30 UTC and 23:00 UTC all calculated positions are situated in regions where the mean brightness temperature (within a square of edge length = 30 km centered at the respective position) ranged between −30 and −20°C with standard deviations of 1–2 K. As the temperatures of the considered air parcels were much colder (−35 to −45°C) we can assume that they were cloud free during that time.

At 23:30 UTC (the date of the radiosonde ascent) the situation changed: The mean brightness temperatures at the positions of the considered air parcels decreased to significantly lower values ($-40 \leq \overline{T} \leq -35$°C) and their standard deviations increased to values of 5–7 K. The METEOSAT imagery at later times (Fig. 4) shows even lower brightness temperatures at the air parcels' positions. This evolution suggests that during the radiosonde ascent a (cirrus) cloud began to form in the ice supersaturated region that became opaque within about 2 h.

Before we estimate the properties of the cloud that formed while the radiosonde ascended we take a look at the whole scene. The reason is that the brightness temperature did nowhere reach higher values than −15°C even at places where no clouds are evident on the corresponding infrared image obtained by AVHRR (Fig. 5). However, the AVHRR image seems to display a feathery veil over locations where one can see the ground. This suggests that a horizontally extended cirrus cloud is present below the tropopause. The optical thickness of this cirrus can be estimated using the simple radiative transfer equations from Case 1. Using the radiosonde profiles from 20 March 2000, 18:00 UTC, and ECMWF profiles at the positions of the main trajectories at that time we find a very humid layer between 210 and 170 hPa, above a rather dry lower and middle troposphere. Whereas the METEOSAT brightness temperature ranged between −26 and −21°C, the temperature of the "cirrus" layer was about −68°C and the surface temperature can be estimated as $T_{surf} \approx 1.3$°C. These values result in an estimate of optical depth in the range $0.31 \leq \tau \leq 0.43$ at the wavelength $\lambda = 11.5\,\mu$m.

ACPD
5, 67–100, 2005

Now we return to the cirrus that formed in the ice-supersaturated region just at the time of the radiosonde's ascent over Lindenberg. The optical thickness of this cloud (at about $p \approx 340$ hPa) can be calculated from a slight generalisation of the equations derived in Case 1, where we have to take into account not only the cloud itself (subscript 2 in the formula below) and the underlying surface or boundary layer clouds, but additionaly the cold cirrus at the tropopause (subscript 1). In this situation and with the simplifying assumptions of Case 1, the radiance measured by a satellite is:

$$I_{\text{sat}} = B_\lambda(T_1)(1 - e^{-\frac{\tau_1}{\mu}}) + \left(B_\lambda(T_{\text{surf}})e^{-\frac{\tau_2}{\mu}} + B_\lambda(T_2)(1 - e^{-\frac{\tau_2}{\mu}})\right) e^{-\frac{\tau_1}{\mu}}, \quad (2)$$

with the Planck function B_λ for wavelength λ at the temperatures of the clouds $T_{1,2}$ and the underlying surface T_{surf}. The factor $1/\mu$ corrects the vertically measured optical thickness for the slanted viewing geometry: μ is the cosine of the zenith distance of the satellite seen from Lindenberg, which is equivalent to the geographical latitude of that location. The brightness temperature is defined as $I_{\text{sat}}=B_\lambda(T_{\text{br}})$. Then the optical depth τ_2 of the lower cloud is:

$$\tau_2 = \mu \cdot \left[\log\left((B_\lambda(T_{\text{surf}}) - B_\lambda(T_2))e^{-\frac{\tau_1}{\mu}}\right) - \log\left(B_\lambda(T_{\text{br}}) - B_\lambda(T_2)e^{-\frac{\tau_1}{\mu}} - B_\lambda(T_1)(1 - e^{-\frac{\tau_1}{\mu}})\right)\right] \quad (3)$$

For the calculation of the optical depth we use the following: At 00:00 UTC the surface temperature equals the temperature of the top of the opaque boundary layer cloud, i.e. $T_{\text{surf}} \approx 3.0$°C. The optical depth of the high cloud is $\tau_1 = 0.37$, the cloud temperature is $T_1 = -68$°C. The cloud temperature of the lower cloud can be estimated using the temperature profile (radiosonde) as $T_2 = -42.33$°C, i.e. the mean temperature within the top 400 m of the cloud. There is no qualitative difference if we use for T_2 the cloud top temperature $T = -44$°C for our calculations. Since the brightness temperatures were changing considerably from 00:00 UTC on, we compute a range of optical thicknesses for the range of brightness temperatures from −30 to −49°C as they occurred in the METEOSAT data. The results are presented in Table 1.

ACPD
5, 67–100, 2005

Additionally, we calculate the ice water content (IWC) for the two cirrus clouds (cf. Case 1):

$$\mathrm{IWC} = \frac{\tau}{\beta \cdot \Delta z \cdot \left(\alpha_i + \frac{\gamma_i}{r_{\mathrm{eff}}}\right)} \,. \tag{4}$$

First, we estimate the ice water content for the higher cirrus. From the radiosonde profile we find a thickness of the cloud layer of about 2 km. From Ebert and Curry (1992) we take the constants α_i=0.0016 $\mathrm{m^2\,g^{-1}}$, γ_i=1.166 $\mathrm{m^2\,g^{-1}\,\mu m^{-1}}$ and β=1.66. Because of the very low temperatures inside the cirrus layer ($-71 \leq T \leq -58^{\circ}$C) we can assume a small effective radius of the ice crystals, for our calculation we set r_{eff}=10 μm. Then, for an optical depth within $0.31 \leq \tau_1 \leq 0.43$ we obtain an IWC between 0.80 and 1.11 $\mathrm{mg\,m^{-3}}$. The total water content inside this layer can be estimated as about 5.3–6.2 $\mathrm{mg\,m^{-3}}$. The empirical formula of Schumann (2002),

$$\mathrm{IWC}(T) = \exp\left(6.97 + 0.103 \cdot T(^{\circ}\mathrm{C})\right) \frac{\mathrm{mg}}{\mathrm{m^3}}, \tag{5}$$

gives for a mean temperature inside the cloud layer of about -65°C a mean IWC of 1.3 $\mathrm{mg\,m^{-3}}$ which is consistent with the values obtained from the calculation by using the optical depth τ_1.

Inside the lower, just forming cirrus cloud we find a much larger variability of the brightness temperatures that is due to the quick evolution of this cloud. This also implies a larger uncertainty in our estimates. For 23:30 UTC when the cloud is just forming, we assume r_{eff} is between 10 and 20 μm. But later, at 01:30 UTC, when the cloud approaches equilibrium (i.e. saturation), we assume larger ice crystals with r_{eff} between 30 and 50 μm. We also have to take into account the variation of the optical thickness (see Table 1): For 23:30 UTC we consider the lower values of τ_2 (0.235 to 0.763) as relevant, and for 01:30 UTC the higher values (0.640 to 1.444), because the cloud became opaque. The thickness of the ice supersaturated layer was $\Delta z \approx 1600$ m. With this input we estimate $0.74 \leq \mathrm{IWC} \leq 4.7$ $\mathrm{mg\,m^{-3}}$ for 23:30 UTC and

$4.0 \leq \mathrm{IWC} \leq 21.8\,\mathrm{mg\,m^{-3}}$ for 01:30 UTC. The temperature inside the cloud layer ranged from −44 to −31.2°C, the mean value is $\overline{T} = -37.4$°C. Hence, the formula of Schumann (2002) gives $11.5 \leq \mathrm{IWC}(T) \leq 42.8\,\mathrm{mg\,m^{-3}}$ and $\mathrm{IWC}(\overline{T}) = 22.6\,\mathrm{mg\,m^{-3}}$. These values are in good accordance to the values calculated from the optical thicknesses for 01:30 UTC. At this time the cirrus cloud was probably close to equilibrium which is a condition for the validity of the formula of Schumann (2002).

The total water concentration in the supersaturated layer can be estimated from the specific humidity profile determined from the radiosonde data: $\overline{q}_{\mathrm{tot}} = 180\,\mathrm{mg\,m^{-3}}$. Hence, the ice phase consisted of about 0.4 to 2.2% of the total water at 23:30 UTC when the cirrus was just forming. Later when the cloud approached equilibrium, about 2 to 12% of the total water was in the ice phase. This is much less than we would estimate for a cirrus forming by homogeneous nucleation.

3.4. Mesoscale simulation

3.4.1. Model setup

The mesoscale fields are calculated with the non-hydrostatic weather prediction model MM5-version 3.4 (Dudhia, 1993; Dudhia et al., 2001). The outer model domain is centred at (52° N, 10° E) with an extension of 4401 km×4401 km. In this domain a horizontal grid size of $\Delta x = 27$ km is used. A local grid refinement scheme with a nested domain of 9 km horizontal resolution is applied to resolve most of the horizontal wavenumber spectrum of gravity waves excited either by the orography or by jet stream instabilities. The model has 200 vertical levels up to the model top at 10 hPa ($\Delta z \approx 150$ m) are applied. Turbulent and moist processes are accounted for by standard schemes as the Hong and Pan (1996) turbulence scheme, commonly referred as MRF scheme, Grell's cumulus parameterization (Grell et al., 1994) and Reisner's microphysical scheme (Reisner et al., 1998). The initial condition at 20 March 2000 12:00 UTC and the boundary values of the model integration are prescribed by operational analyses from the ECMWF model with a horizontal resolution of 0.5° in latitude and longitude

and 15 pressure levels between the surface and the 10 hPa pressure level.

3.4.2. Results

Results of the mesoscale model simulation confirm the hypothesis of ascending air between 7 and 10 km altitude near Lindenberg induced by internal gravity waves. Figure 6 details the meteorological situation at the 318 K isentropic surface (≈9 km altitude) at 21 March 2000, 01:00 UTC (cf. Fig. 1). As at 500 hPa, the large-scale upper-tropospheric flow is dominated by the ridge over northern Germany and the anticyclonically curved jet stream. However, mesoscale perturbations seen as vertical wind fluctuations appear in two areas north and south of Lindenberg (Fig. 7).

Coherent wave packets with a horizontal wavelength $\lambda_x \approx 200$ km are simulated at the north-eastern edge of the ridge. They extend from Lindenberg over the Baltic Sea toward southern Sweden (Fig. 6). In this region, the maximum curvature of the jet causes a strongly unbalanced flow regime which is subject to inertial instability. Inertia-gravity waves are excited on the anticyclonic side of the jet stream. This simulation result is in accordance with former studies showing that strongly diffluent regions are preferred locations for the excitation of inertia-gravity waves (Knox, 1997; Plougonven et al., 2003; Peters et al., 2003). Due to the wrapping of the anticyclonically breaking Rossby wave, the simulated inertia-gravity wave packets propagate with the excitation region and get strongly dispersed in the curved flow.

The hodograph analysis of the radiosonde profile of the 21 March 2000 00:00 UTC sounding shows a cyclonic rotation of the wind vector with height between 8 and 11 km altitude (Fig. 8). This indicates a downward propagating gravity wave (Gill, 1982). Hence, the gravity wave source is located in the upper troposphere in accord with the simulated mesoscale flow. The wave parameters can be determined by fitting the hodograph with the linear polarization relationship of inertia-gravity waves

$$u' = \hat{u}\, R(\Theta) \cos(mz + \Phi) \qquad (6)$$

ACPD
5, 67–100, 2005

$$v' = -\hat{u}\, R(\Theta)\, \frac{f}{\omega_0}\, \sin(mz + \Phi), \tag{7}$$

where $\hat{u}$ is the amplitude of the wave, m and ω_0 are its vertical wavenumber and intrinsic frequency, and f is the Coriolis parameter (Thompson, 1978). The matrix $R(\Theta)$ rotates the reference frame in such a way that the phase speed of the wave is parallel to the x-axis. The polarization relationship states that the ratio between the long and short ellipse axes is equal to ω_0/f. From Fig. 8, we find ω_0=2.8 f, a typical value for an inertia gravity wave. The result of the fit with $\hat{u}$=0.5 m s^{-1} gives a vertical wavenumber m=3.8 10^{-3} m^{-1}, i.e. the vertical wavelength is small: $\lambda_z \approx$1.6 km. The horizontal wave number is determined from the dispersion relationship

$$m^2 = \frac{N^2 - \omega_0^2}{\omega_0^2 - f^2} \left(k^2 + l^2\right) \tag{8}$$

with N as the buoyancy frequency and knowing that tan $\Theta = |l/k|$. In our case Θ=45°, so l=k. The estimates of the horizontal wavelength λ_h range from 120 km for N=0.015 s^{-1} to 200 km for N=0.025 s^{-1}. Although the hodograph method has uncertainities (Zhang et al., 2004), our estimates agree very well with the values of the mesoscale numerical simulation.

The other area of mesoscale flow perturbations is located south of Lindenberg. There, surface winds of ≈10 m s^{-1} past the Erzgebirge and Riesengebirge excite vertically propagating mountain waves with λ_h<100 km that produce a quasi-stationary wave pattern at the south-east edge of the high pressure ridge. Although the maximum vertical velocities directly above the mountains exceed 0.5 m s^{-1} the magnitude of the vertical wind in a distance of 150 km south of Lindenberg is similar to the amplitude in the inertia-gravity waves.

The vertical section in Fig. 7 reveals the different spatial structure of the simulated inertia-gravity waves north and the mountain waves south of Lindenberg. In Fig. 7 the inertia gravity wave pattern appears as nearly horizontal band of up- and downdrafts

ACPD
5, 67–100, 2005

with maximum vertical velocities of about 10 cm s^{-1} above and north of Lindenberg whereas the mountain waves propagate from below.

Figure 9 shows a series of pseudo-soundings (i.e. vertical profiles at a grid point) specific humidity at Lindenberg, using the MM5 output for times between −6 and +6 h around the reference time. One realizes that the later soundings appear as upward shifted versions of the earlier soundings, which means that on a fixed pressure level the specific humidity increases with time as a result of moist advection from below. Trajectories based on the MM5 wind fields show an overall upward motion (with intermittent downward excursions) in the upper troposphere over and around Lindenberg before the observation of the ISSR (Fig. 10).

Both wave systems, the mountain wave and the jet-stream induced inertia-gravity wave superimpose in an area of about 300 km×300 km around Lindenberg leading to an uplift of moist air masses from below and to the formation of the wave-induced ISSR and the cirrus cloud.

4. Ice supersaturation on isobaric surfaces

In order to visualise the horizontal extension of the studied ice-supersaturated region we employ the technique that we have introduced in Case 1. We do this both for the ice-supersaturated region that the radiosonde detected at 0 h and, additionally, for the humid layer with the extended thin cirrus just below the tropopause.

In the present case (Fig. 11), the ECMWF model underestimated the relative humidity by a large amount, it had RHi=92% where the radiosonde gave values in excess of 110%. Hence, even ECMWF RHi-values as low as 70% may actually have been supersaturated. Aside from the ISSR over Lindenberg the map, representing the pressure surface p=389 hPa, shows other moist regions which are independent of the one over Lindenberg and which generally last for longer times. As these ice-supersaturated regions were situated 100 to 200 hPa below the tropopause, there is no apparent correlation between their boundaries and the isolines of poten-

tial vorticity (PV=1.6, 2.5, 3.5 PVU). Again, as in Case 1 we find in a plot log(area) vs. log(perimeter) a slope of less than 2, that is, a signature for the fractal geometry of the ISSRs.

An analogous calculation is performed for the tropopause cirrus, for which we investigate the humidity field and its gradients on the pressure surfaces p=202 and p=204 hPa. The horizontal extensions of the (probably) supersaturated regions are shown in Fig. 12. During the time interval between t=−6 h and t=+12 h an ice supersaturated layer can be seen over Germany, which is slowly disappearing. The boundary of this ISSR is closely followed by the PV-contours, reflecting the situation of this region just below the tropopause.

5. Conclusions

In this case study we have analysed the formation and evolution of an ice-supersaturated region that has been detected by a radiosonde over Lindenberg on 21 March 2000, 00:00 UTC. The sonde reported supersaturation in the pressure range 320.6≤p≤408.2 hPa. We have analysed this case using satellite data (METEOSAT IR imagery and AVHRR data), simple radiative transfer calculations, trajectory calculations based on operational ECMWF analyses, and mesoscale numerical simulations.

We found that in this case the generation of supersaturation was due to a lifting of airmasses by about 20 to 40 hPa that was caused by a superposition of two packets of gravity waves, one generated by air flow past the Erzgebirge, Riesengebirge and the other excited by inertial instability on the north-eastern edge of an anticyclone. The lifting led to a strong increase of specific humidity (by factors 1.5 to 1.75), while the temperature decreased only little. The generated wave-induced ISSR lasted only for half a day or so and vanished with the decaying wave activity. The region had a vertical extension of about 2 km, which is almost 4 times the average thickness of ice supersaturation layers found in the Lindenberg radiosonde profiles (about 500 m, see Spichtinger et al., 2003a). Over Lindenberg the lifting of the air not only led to supersat-

uration, but it also triggered the formation of a cirrus cloud that became optically thick within about 2 h. The whole region was covered by another, still higher and more long-lasting, optically thin cirrus just below the tropopause where the radiosonde reported high relative humidities, yet below 100%.

In this case the generation of supersaturation was dominated by moisture advection (from below), while in Case 1 the cooling and hence the decrease of the saturation water vapour pressure was the prevailing generation mechanism. Whereas in Case 1 the lifetime of the supersaturated region exceeded a da (more precisely one should say that the tracked air parcels were part of the ISSR for more than a day, the ISSR itself lasted considerably longer), in the present case it was only about half a day. Whether this is systematic, that is, whether supersaturation generated by moisture advection due to small scale vertical air motion lasts on average shorter than cooling generated supersaturation, is not known, but it could be the case.

We also have seen that the considered ISSR appeared over a larger area where other ISSRs were already present and which also still were around when our ISSR was already disappearing. Unfortunately, we had to use recalculated humidity fields to visualise the ISSRs because the ECMWF model itself does not allow supersaturation. This is something that should be improved, and we are currently working on an improved cloud scheme in the ECMWF model that allows ice-supersaturation in the upper troposphere to exist. We hope that inclusion of ISSRs in large scale models will contribute to an improvement of the representation of cirrus clouds and their radiative properties which would be of great value for weather forecasts and for studies of climate change. Furthermore, we are going to conduct mesoscale numerical simulations of the upper troposphere in order to study the formation and evolution of ice-supersaturated regions together with their embedded cirrus clouds in more detail.

ACPD
5, 67–100, 2005

Appendix

In Case 1 we analysed how relative humidity changes along a trajectory due to the respective changes in temperature, specific humidity, and pressure:

$$dRHi = \frac{\partial RHi}{\partial T} dT + \frac{\partial RHi}{\partial q} dq + \frac{\partial RHi}{\partial p} dp. \quad \text{(A1)}$$

While the temperature contribution dominated for Case 1, the ECMWF based trajectories for the present case suggest that the moisture term dominates. However, the temperature evolution along the mesoscale trajectories shows that this is not true. Hence, the temperature effect due to the mesoscale gravity waves is responsible for the humidity increase and, eventually, for the formation of the cloud. This contradiction between ECMWF analyses and the MM5 simulation results indicates that the time interval between the individual analyses times is too long to resolve the true motion of the air parcels. Let us analyse this a bit further.

For this analysis it turns out it is better to use the (extensive quantity) water vapour partial density ρ_v instead of (the intensive quantity) q (q=ρ_v/ρ with air density ρ). Then we write:

$$\frac{dRHi}{dt} = \frac{\partial RHi}{\partial T}\frac{dT}{dt} + \frac{\partial RHi}{\partial \rho_v}\frac{d\rho_v}{dt}. \quad \text{(A2)}$$

The total derivative $d\rho_v/dt$ can be rewritten in the following way:

$$\frac{d\rho_v}{dt} = \frac{\partial \rho_v}{\partial t} + (\mathbf{v}\cdot\nabla)\rho_v \quad \text{(A3)}$$

$$= \frac{\partial \rho_v}{\partial t} + \nabla\cdot(\mathbf{v}\rho_v) - \rho_v \nabla\cdot\mathbf{v} \quad \text{(A4)}$$

$$= Q - \rho_v \nabla\cdot\mathbf{v}. \quad \text{(A5)}$$

For ρ_v the continuity equation holds, and only when there are cloud processes or chemical processes involving water molecules, the source term Q is different from zero.

ACPD
5, 67–100, 2005

The budget equation along a trajectory is now:

$$\frac{dRHi}{dt} = \frac{\partial RHi}{\partial T}\frac{dT}{dt} + \frac{\partial RHi}{\partial \rho_v}(Q - \rho_v \nabla \cdot \mathbf{v}). \quad \text{(A6)}$$

We could now re-introduce the specific humidity and would arrive at a similar equation with q replacing ρ_v (and with an accordingly re-defined source term Q' and term involving the pressure re-included).

Often, the atmosphere can be regarded as an incompressible medium, such that $\nabla \cdot \mathbf{v}$=0. This means that, unless there is a non-vanishing source term Q (e.g. cloud formation), the contribution of the moisture term to the evolution of the relative humidity along a Lagrangian trajectory should vanish (see also Stohl and Seibert, 1998). The large q-change along the trajectories based on 6 hourly ECMWF analyses indicates a failure determining parcel properties along the trajectory. Not only the temporal resolution is too coarse but also the excitation of inertia-gravity waves is not resolved by the ECMWF model for this particular case.

Acknowledgements. We thank R. Meyer and R. Büll for processing and providing the METEOSAT data and H. Wernli for providing the model LAGRANTO and for some fruitful discussions. The mesoscale numerical simulations were performed on the NEC SX6 computer at the German High Performance Computing Center for Climate and Earth System Research in Hamburg, Germany. The analysis data were kindly provided by ECMWF for the special project "Ice supersaturation and cirrus clouds". This article contributes to COST action 723 (Data exploitation and modeling for the upper tropopshere and lower stratosphere) and to the DLR/HGF-project "Particles and Cirrus Clouds" (PAZI-2).

References

Dudhia, J.: A non-hydrostatic version of the Penn State-NCAR Mesoscale Model: Validation tests and simulation of an Atlantic cyclone and cold front, Mon. Wea. Rev., 121, 1493–1513, 1993. 70, 78

Dudhia, J., Gill, D., Guo, Y.-R., Manning, K., and Wang, W.: PSU/NCAR Mesoscale Modeling System Tutorial Class Notes and User Guide: MM5 Modeling System Version 3, 2001, available at http://www.mmm.ucar.edu/mm5/documents/MM5_tut_Web_notes/TutTOC.html. 70, 78

Ebert, E. E. and Curry, J. A.: A parameterization of cirrus cloud optical properties for climate models, J. Geophys. Res., 97, 3831–3836, 1992. 77

Gierens, K., Schumann, U., Helten, M., Smit, H. G. J., and Marenco, A.: A distribution law for relative humidity in the upper troposphere and lower stratosphere derived from three years of MOZAIC measurements, Ann. Geophys., 17, 1218–1226, 1999, SRef-ID: 1432-0576/ag/1999-17-1218. 68

Gill, A. E.: Atmosphere-Ocean Dynamics, Academic Press New York, 1982. 79

Grell, G. A., Dudhia, J., and Stauffer, D. R.: A description of the fifth-generation Penn State/NCAR mesoscale model (MM5), NCAR Technical Note, NCAR/TN-398+STR, 117,1994. 78

Hong, S.-Y. and Pan, H.-L.: Nonlocal boundary layer vertical diffusion in a medium-range forecast model, Mon. Wea. Rev., 124, 2322–2339, 1996. 78

Knox, J. A.: Possible mechanism of clear-air turbulence in strongly anticyclonic flow, Mon. Wea. Rev., 125, 1251–1259, 1997. 79

Peters, D. and Waugh, D. W.: Influence of barotropic shear on the poleward advection of upper-tropospheric air, J. Atmos. Sci., 53, 3013–3031, 1996. 69

Peters, D., Hoffmann, P., and Alpers, M.: On the appearance of inertia-gravity waves on the north-easterly side of an anticyclone, Meteorol. Z., 12, 25–35, 2003. 79

Plougonven, R., Teitelbaum, H., and Zeitlin, V.: Inertia gravity wave generation by the tropospheric midlatitude jet as given by the Fronts and Atlantic Storm-Track Experiment radio soundings, J. Geophys. Res., 108, 4686, doi:10.1029/2003JD003535, 2003. 79

Reisner, J., Rasmussen, R. J., and Bruintjes, R. T.: Explicit forecasting of supercooled liquid water in winter storms using the MM5 mesoscale model, Q. J. Roy. Meteorol. Soc., 124B, 1071–1107, 1998. 78

Schumann, U.: Contrail Cirrus, in: Cirrus, edited by: Lynch, D. K., Sassen, K., Starr, D. O'C., and Stephens, G., Oxford University press, Oxford, UK, 231–255, 2002. 77, 78

Spichtinger, P., Gierens, K., Leiterer, U., and Dier, H.: Ice supersaturation in the tropopause region over Lindenberg, Germany, Meteorol. Z., 12, 143–156, 2003a. 70, 82

Spichtinger, P., Gierens, K., and Read, W.: The global distribution of ice-supersaturated regions

as seen by the microwave limb sounder, Q. J. Roy. Meteorol. Soc., 129, 3391–3410, 2003b. 68

Spichtinger, P., Gierens, K., and Wernli, H.: A case study of the formation and evolution of ice supersaturation in the vicinity of a warm conveyor belt's outflow region, Atmos. Chem. Phys. Discuss., accepted, 2004. (Case 1) 69

Stohl, A. and Seibert, P.: Accuracy of trajectories as determined from the conservation of meteorological tracers, Q. J. Roy. Meteorol. Soc., 124, 1465–1484, 1998. 74, 85

Thompson, R. O. R. Y.: Observation of inertial gravity waves in the stratosphere, Q. J. Roy. Meteorol. Soc., 104, 691–698, 1978. 80

Wernli, H. and Davies, H. C.: A Lagrangian-based analysis of extrtropical cyclones, I: The method and some applications, Q. J. Roy. Meteorol. Soc., 123, 467–489, 1997. 70

Zhang, F., Wang, S., and Plougonven, R.: Uncertainties in using the hodograph method to retrieve gravity characteristics from individual soundings, Geophys. Res. Lett., 31, L11110, doi:10.1029/2004GL019841, 2004. 80

Table 1. Values of the optical depth τ_2 for different brightness temperatures, calculated by using the Eq. (3).

T_{br} (°C)	−30	−36.5	−40	−42
τ_2	0.235	0.473	0.640	0.755
T_{br} (°C)	−45	−46	−49	
τ_2	0.973	1.063	1.444	

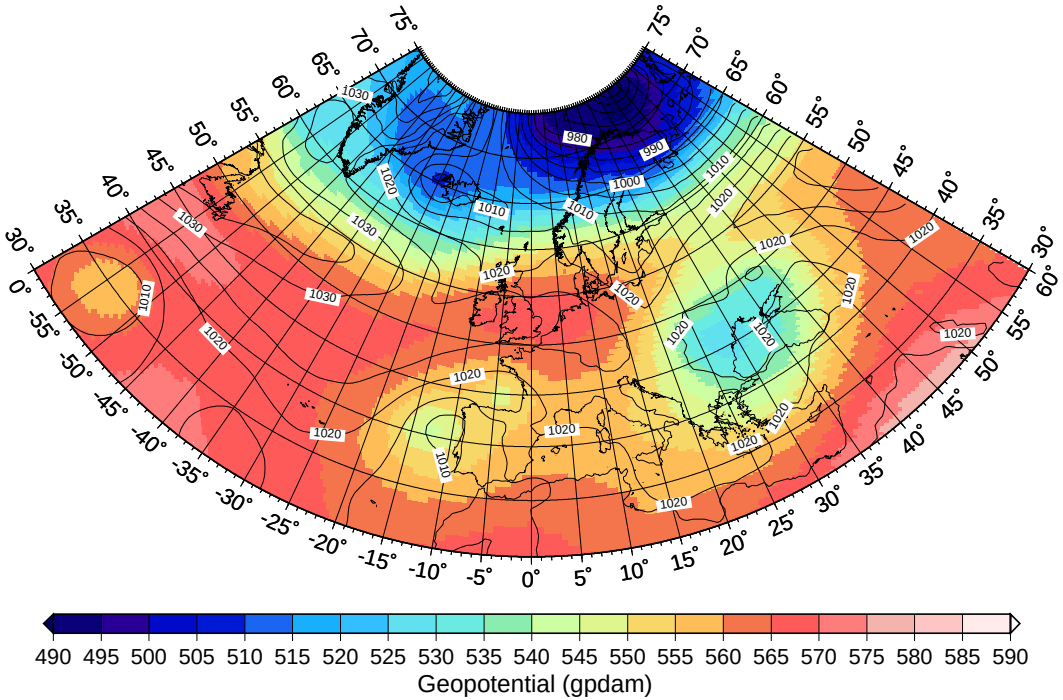

Fig. 1. Geopotential (in gpdam) at 500 hPa and surface pressure (black curves, isobars) for the 21 March 2000, 00:00 UTC.

ACPD

5, 67–100, 2005

Ice supersaturation caused by mesoscale gravity waves

P. Spichtinger et al.

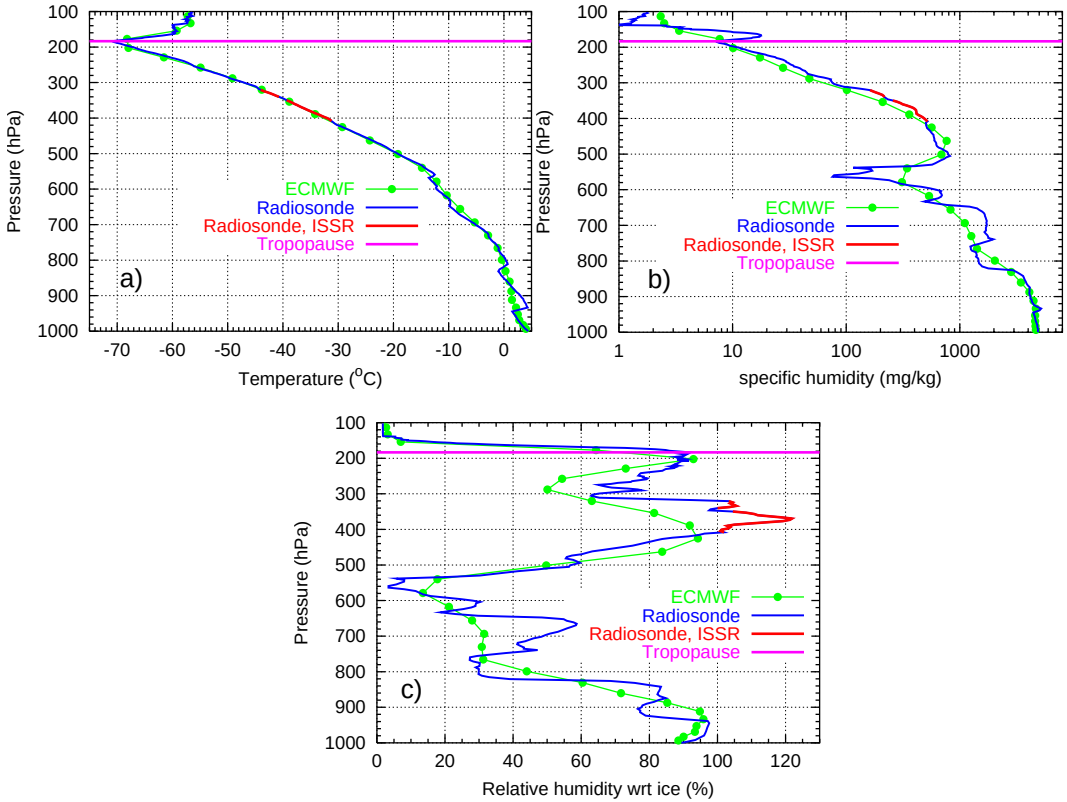

Fig. 2. Vertical profiles of the radiosonde (blue curve) and the corresponding values from the ECMWF data set (green filled circles and curve, values picked from the nearest grid points at every model level). Additionally, the thermal tropopause (pink line) and the reported ice supersaturated layer (red curve) obtained from the radiosonde are shown. **(a)**: temperature in degree Celsius; **(b)**: specific humidity in milligrams water vapour per kilogram dry air; **(c)**: relative humidity with respect to ice in percent.

ACPD
5, 67–100, 2005

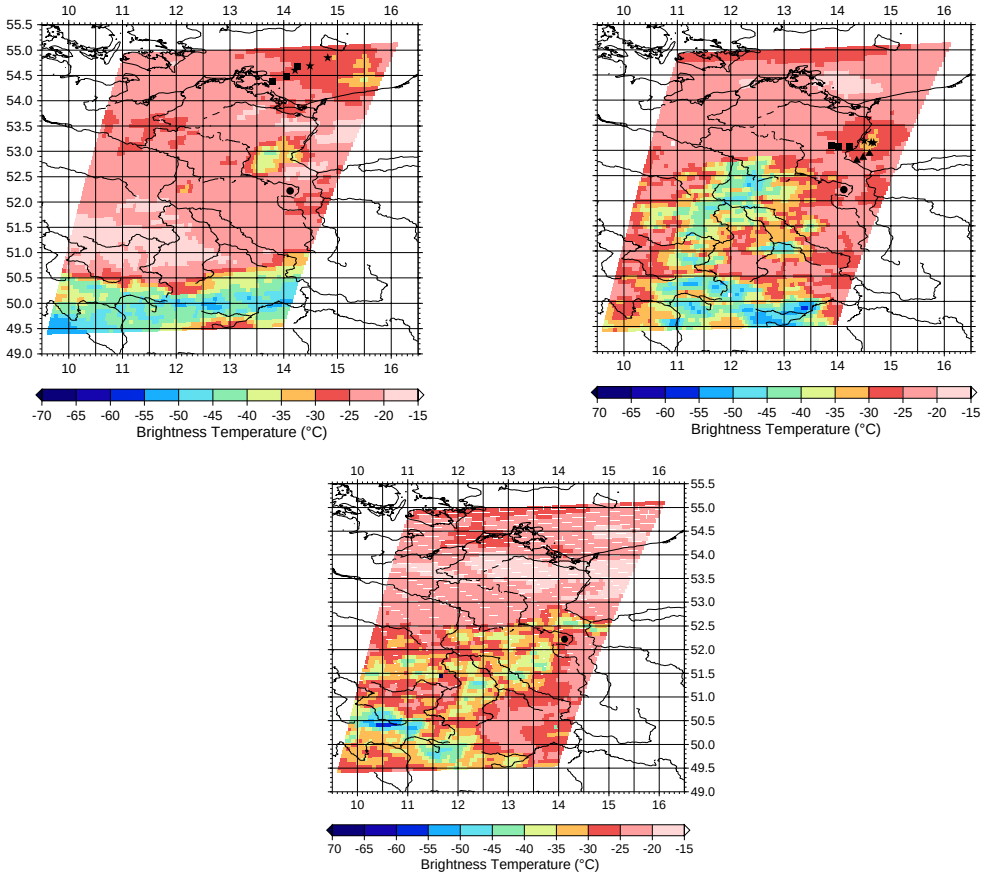

Fig. 3. Infra red METEOSAT image of the region "GermanyNE" at 17:30 UTC (left), 21:30 UTC (middle) and 23:00 UTC (right) on 20 March 2000. Additionally, the positions of Lindenberg (filled circle, 14.12° E/52.22° N), of the main trajectories $Tr_{34,1}-Tr_{36,1}$ (black squares), of the neighbouring trajectories $Tr_{34,5}-Tr_{36,5}$ (black stars) and of the air parcels measured by the radiosonde (black triangles, only for 21:30 UTC and 23:00 UTC) are shown.

ACPD
5, 67–100, 2005

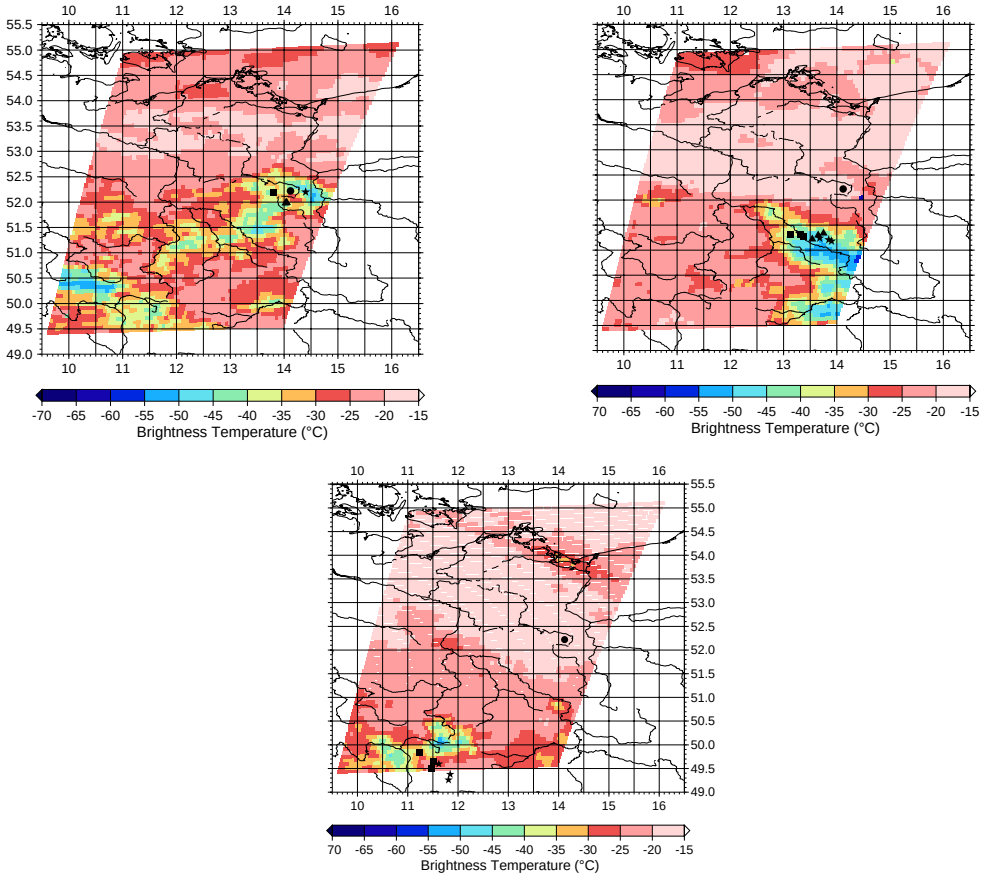

Fig. 4. As Fig. 3, but at 23:30 UTC on 20 March 2000 (left), 01:30 UTC (middle) and 05:30 UTC (right) on 21 March 2000. Additionally, the positions of the air parcels measured by the radiosonde (black triangles, only 23:30 UTC and 01:30 UTC) are shown.

ACPD
5, 67–100, 2005

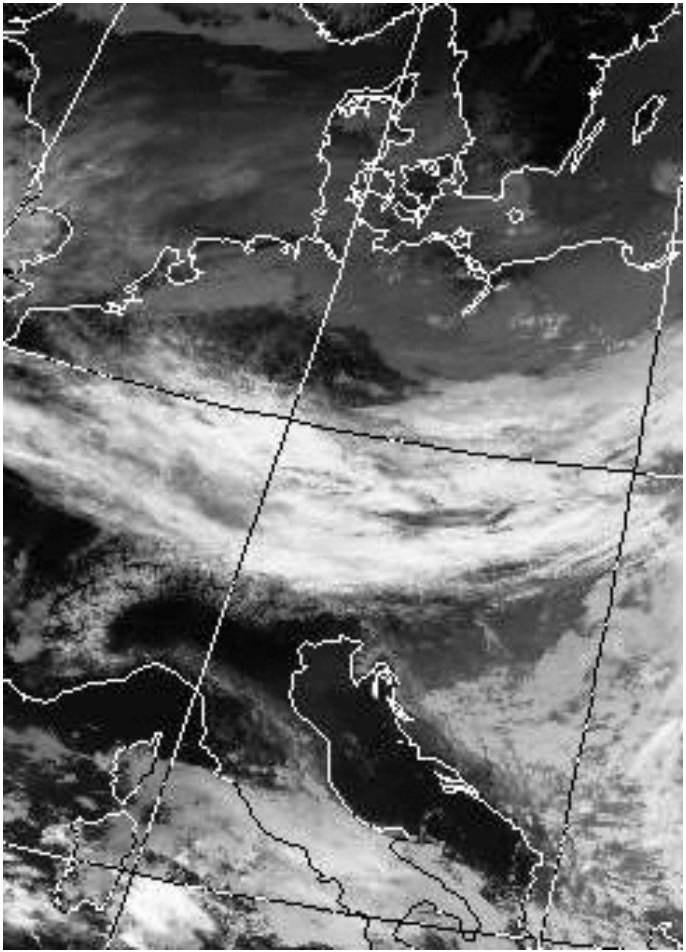

Fig. 5. AVHRR – IR: 20 March 2000, 16:01 UTC, kindly provided by NERC Satellite Receiving Station, Dundee University, Scotland (http://www.sat.dundee.ac.uk/).

ACPD

5, 67–100, 2005

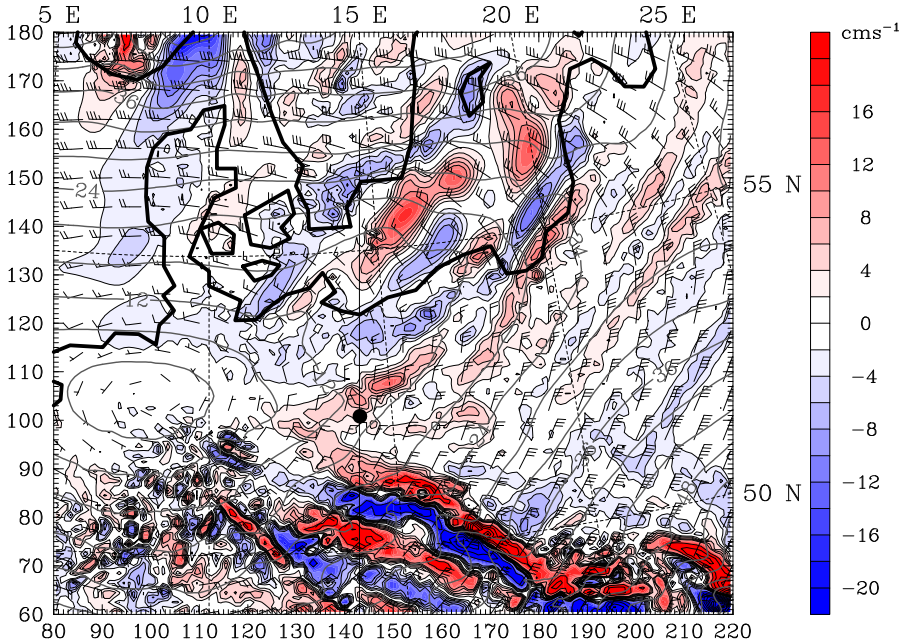

Fig. 6. Vertical velocity (cms^{-1}, color shaded and thin black isocontours with Δw=2 cms^{-1} from 2 cms^{-1} to 10 cms^{-1} and Δw=10 cms^{-1} starting at 20 cms^{-1}) and horizontal wind speed (m/s, barbs; long: 10 ms^{-1}, short 5 ms^{-1}, and gray isocontours with Δu=4 ms^{-1} interval) at the isentropic surface 318 K valid at 21 March 2000 01:00 UTC (+13 h simulation time). The labels denote longitude/langitude (top and right boundary) or number of MM5 grid points (bottom and left boundary), respectively. Numerical results from the innermost domain with Δx=9 km (distance between small tick marks) are shown. The black dot marks the location of Lindenberg and the straight north-south line is the base line of the vertical section in Fig. 7 (the actual start of the line is 20 grid cells to the south).

ACPD
5, 67–100, 2005

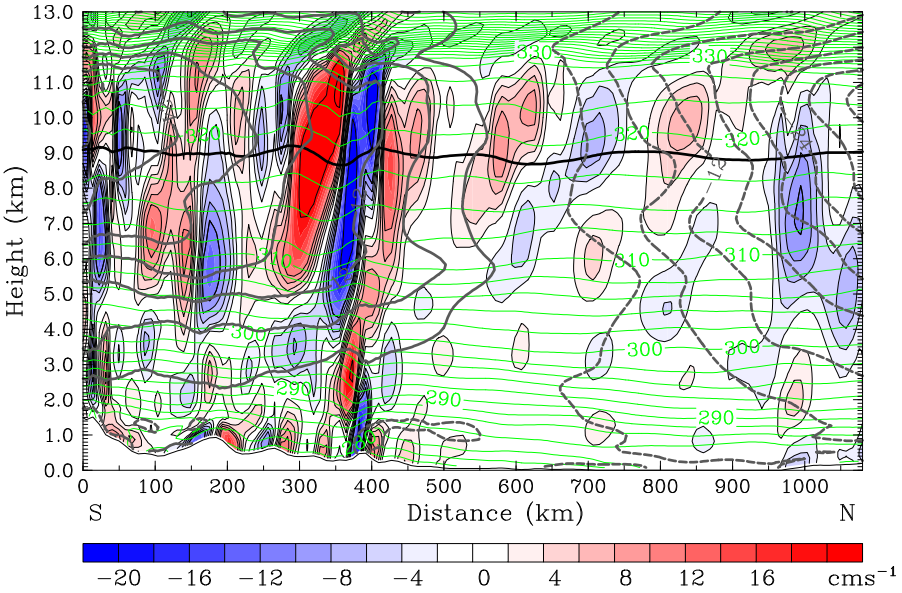

Fig. 7. Vertical velocity (cms^{-1}, scaling as in Fig. 6), potential temperature (K, green isocontours, 2 K increment), and plane normal horizontal wind speed (ms^{-1}, gray isocontours with Δu=4 ms^{-1}, dashed out of, solid into the plane) along the base line indicated in Fig. 6 valid at 21 March 2000 01:00 UTC (+13 h simulation time). The location of Lindenberg is just in the middle of section at about 575 km horizontal distance. The black line at 318 K marks the height of the section in Fig. 6. Numerical results from the innermost domain with Δx=9 km.

ACPD
5, 67–100, 2005

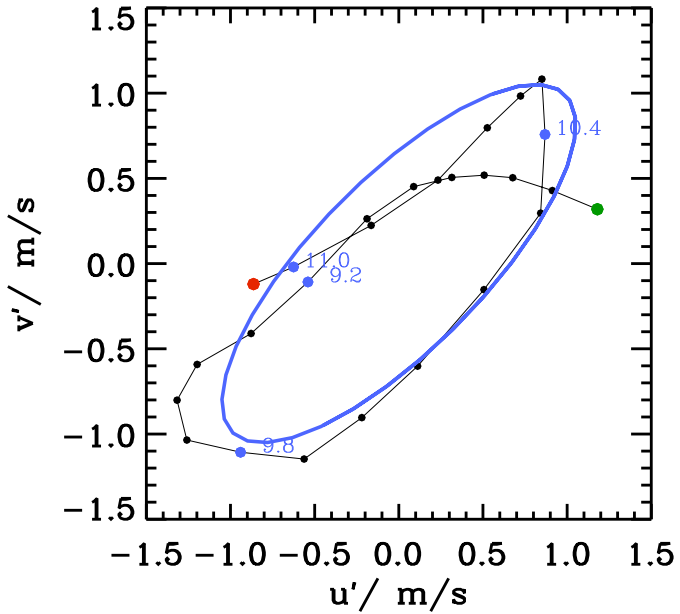

Fig. 8. Hodograph (black) of the zonal u' and meridional v' wind fluctuations between 8 and 11 km generated by the inertia-gravity wave derived from the 21 March 2000 00:00 UTC radiosonde sounding. The blue curve shows the fit of wind fluctuations calculated according to the linear polarization relationship of inertia-gravity waves (see text).

ACPD
5, 67–100, 2005

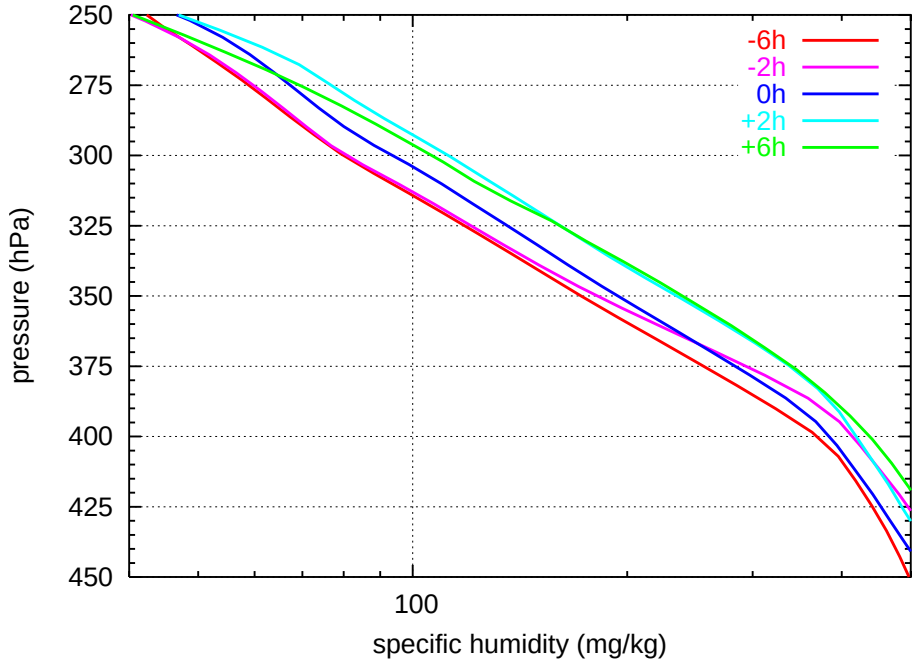

Fig. 9. Pseudo-soundings of specific humidity for various times relative to the reference time, taken from MM5 output at the grid point closest to Lindenberg. Later profiles appear as upward shifted versions of earlier ones.

ACPD
5, 67–100, 2005

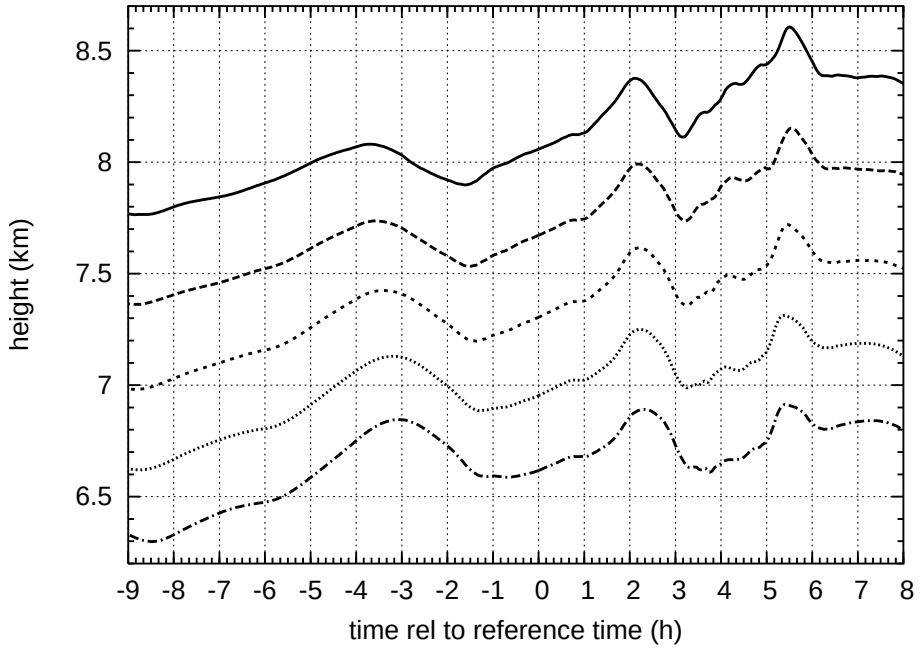

Fig. 10. Altitude variation of trajectories that cross the grid point of Lindenberg at the reference time, computed using the MM5 wind field. Overall, the trajectories ascend, in particular about $t=0$ h, with the exception of some intermittent downward excursions.

ACPD
5, 67–100, 2005

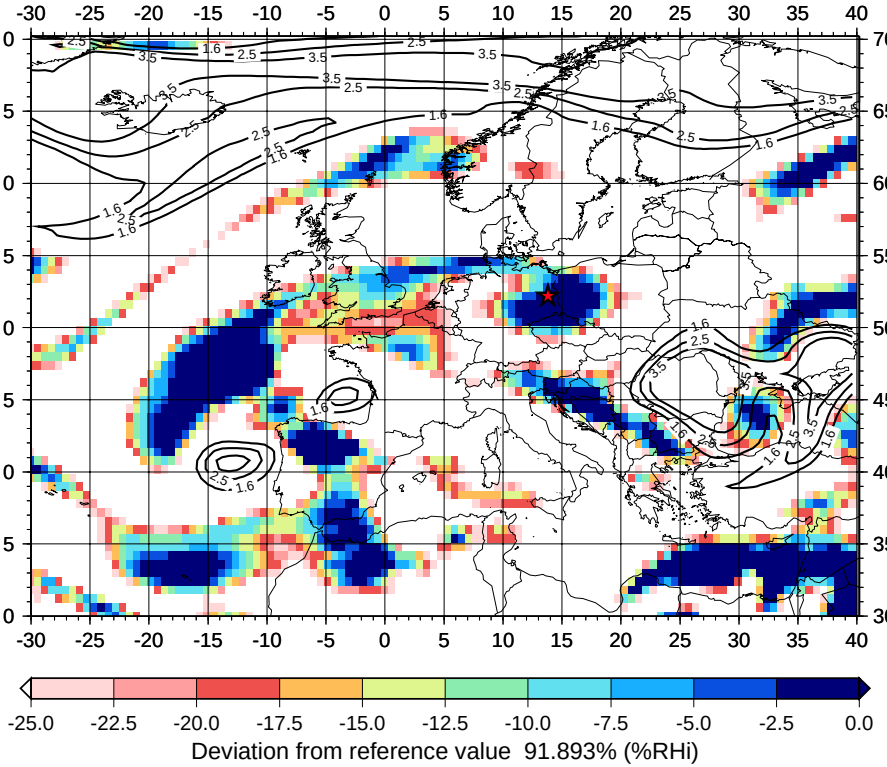

Fig. 11. Visualisation of the ice supersaturated region measured by the radiosonde at 21 March 2000, 00:00 UTC on the pressure surface p=389 hPa, together with other moist regions. The reference value of RHi has been taken from the comparison of the radiosonde and ECMWF data at t=0 h. The position of Lindenberg is marked by a red star. Black contours outline potential vorticities of 1.6, 2.5, and 3.5 PVU.

ACPD
5, 67–100, 2005

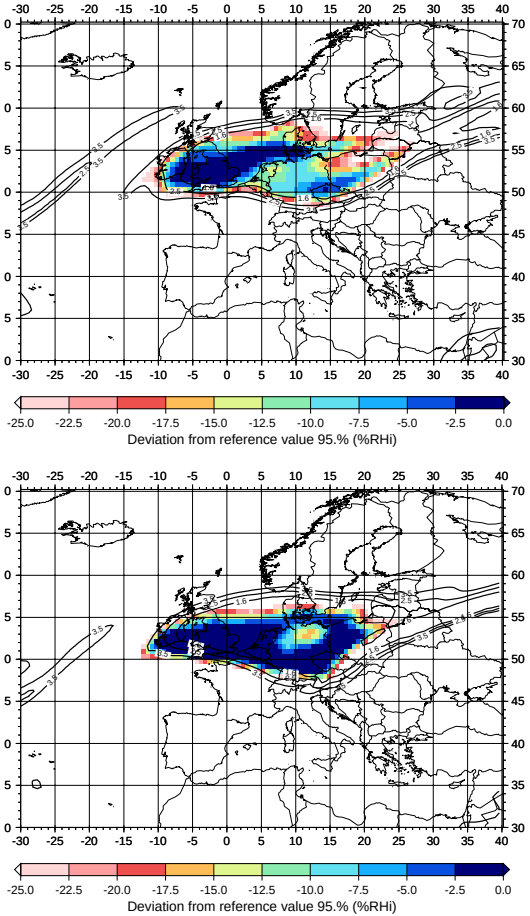

Fig. 12. Evolution of the cirrus cloud situated on the pressure level 30 at $t=-6$ h, $p=204$ hPa and $t=0$ h, $p=202$ hPa. The reference value of RHi is set to $RHi=95.0\%$. Black contours outline potential vorticities of 1.6, 2.5, and 3.5 PVU.

ACPD
5, 67–100, 2005